

High-frequency microrheology reveals cytoskeleton dynamics in living cells

Annafrancesca Rigato, Atsushi Miyagi[†], Simon Scheuring[†] and Felix Rico^{*}

Living cells are viscoelastic materials, dominated by an elastic response on timescales longer than a millisecond¹. On shorter timescales, the dynamics of individual cytoskeleton filaments are expected to emerge, but active microrheology measurements on cells accessing this regime are scarce². Here, we develop high-frequency microrheology experiments to probe the viscoelastic response of living cells from 1 Hz to 100 kHz. We report the viscoelasticity of different cell types under cytoskeletal drug treatments. On previously inaccessible short timescales, cells exhibit rich viscoelastic responses that depend on the state of the cytoskeleton. Benign and malignant cancer cells revealed remarkably different scaling laws at high frequencies, providing a unique mechanical fingerprint. Microrheology over a wide dynamic range—up to the frequency characterizing the molecular components—provides a mechanistic understanding of cell mechanics.

Living cells constantly exert and sense mechanical forces. The magnitude and rate of these forces vary according to organ, tissue and function, modulating the mechanical phenotype of cells. Cells' mechanical response is mainly due to the structural organization and dynamics of individual components of the cytoskeleton. This complex filament network, immersed in a crowded cytoplasm constantly perturbed by molecular motors, displays viscoelastic behaviours³. Consequently, cells exhibit elastic (conservative) and viscous (dissipative) responses that are frequency-dependent. Microrheology quantifies the viscoelastic response by measuring forces in response to deformations⁴ (active microrheology), or by tracking the spontaneous fluctuations of embedded or endogenous particles⁵ (passive microrheology). Viscoelastic properties are then quantified by a frequency-dependent complex shear modulus $G^*(f) = G'(f) + iG''(f)$, where $i = \sqrt{-1}$, and G' and G'' are the elastic and viscous moduli, respectively. Although different cell types show characteristic absolute values of G^* (~ 10 Pa– ~ 100 kPa), general scaling laws describe the mechanical response of living cells; both the elastic and viscous components increase with frequency. At long timescales (low frequencies: 0.01 Hz–100 Hz), live cell active and passive microrheology have shown that G' and G'' are coupled, with a loss tangent $\eta = G''/G' \sim 0.3$, and G^* following a weak power law, with an exponent between 0.05 and 0.35 (refs 1,6). This response has been interpreted in terms of phenomenological soft glassy theories⁴. At higher frequencies (100 Hz– ~ 1 kHz) G^* is expected to show a stronger frequency dependence, with G'' eventually dominating over G' . While a first explanation attributed this to a purely viscous contribution of the cytoplasm, a more mechanistic interpretation involves relaxation modes of individual cytoskeleton filaments, which emerge at high frequencies⁷, as suggested by passive microrheology experiments on reconstituted

cytoskeleton solutions^{8–11}. In such systems, G^* grows with frequency from an elastic plateau to a strong power-law regime^{12–15}. The exponent of the power law is condition-dependent and, in living cells, still a matter of debate due to the scarcity of data^{2,16,17}. Passive microrheology accesses short timescales (~ 10 μ s), but assumes equilibrium conditions to estimate G^* (ref. 15). While active microrheology is suitable for probing the viscoelasticity of out-of-equilibrium systems, such as living cells, it unfortunately operates at frequencies < 1 kHz, without accessing the fast dynamic regime where single cytoskeleton filament dynamics prevail^{2,18}. While some atomic force microscopy works report measurements on cells at a few tens of kHz, their application has been limited to the eigenmode frequencies of the cantilever^{19,20}. In this work, we adapted high-speed atomic force microscopy (high-speed-AFM; ref. 21) and performed active high-frequency microrheology on living cells from 1 Hz to 100 kHz. This widens the explored dynamic range by two orders of magnitude, comprising the expected dynamic regime of cytoskeleton filaments. Our data suggest the existence of at least two regimes: at low frequencies, the cell's dynamic structural elements at the mesoscale lead to a weak power law; at high frequencies, single filament dynamics emerge, revealing stronger power laws that depend on cell type and state. Interpretation in terms of single filament theories of the viscoelastic response at high frequencies provides a mechanistic description of the cytoskeleton of live cells.

We adapted high-speed-AFM with a miniature piezoelectric element with resonance frequency 200 kHz and a high-frequency acquisition board (see Methods and Supplementary Fig. 2). Microcantilevers with resonance frequency 600 kHz in liquid and a spherical tip grown at the end were used to perform active microrheology in the frequency range 1 Hz–100 kHz (Fig. 1b–d and Supplementary Information). The reduced dimensions of high-speed-AFM cantilevers (7 μ m by 2 μ m) provided a viscous drag coefficient of ~ 0.04 pN μ m⁻¹ s (ref. 22), about two orders of magnitude smaller than that of conventional cantilevers^{23,24}, minimizing the required viscous drag correction (Supplementary Fig. 5). Measurements on polyacrylamide gels showed the expected flat plateau of G' at ~ 0.3 kPa up to frequencies ~ 60 kHz, G'' being ~ 10 -fold smaller than G' up to 1 kHz, and showing an upturn at higher frequencies (Supplementary Fig. 7). Previous active and passive microrheology measurements on similar gels are in excellent agreement with our results^{18,25}, confirming the validity of our method. Fibroblasts (NIH-3T3) were directly grown on high-frequency microrheology glass cylinder supports (Fig. 1a) fixed onto a 1.5-mm side beamsplitter, allowing visualization of cells by transmission microscopy, while maintaining the high-frequency capabilities of the z -piezo (Supplementary Fig. 2)²⁶. Measurements were carried out in the perinuclear region to reduce variability and minimize bottom

U1006 INSERM, Aix-Marseille Université, Parc Scientifique et Technologique de Luminy, 163 avenue de Luminy, 13009 Marseille, France. [†]Present address: Departments of Anesthesiology, Physiology and Biophysics, and Biochemistry, Weill Cornell Medical College, 1300 York Ave, New York, New York 10065, USA (A.M., S.S.). *e-mail: felix.rico@inserm.fr

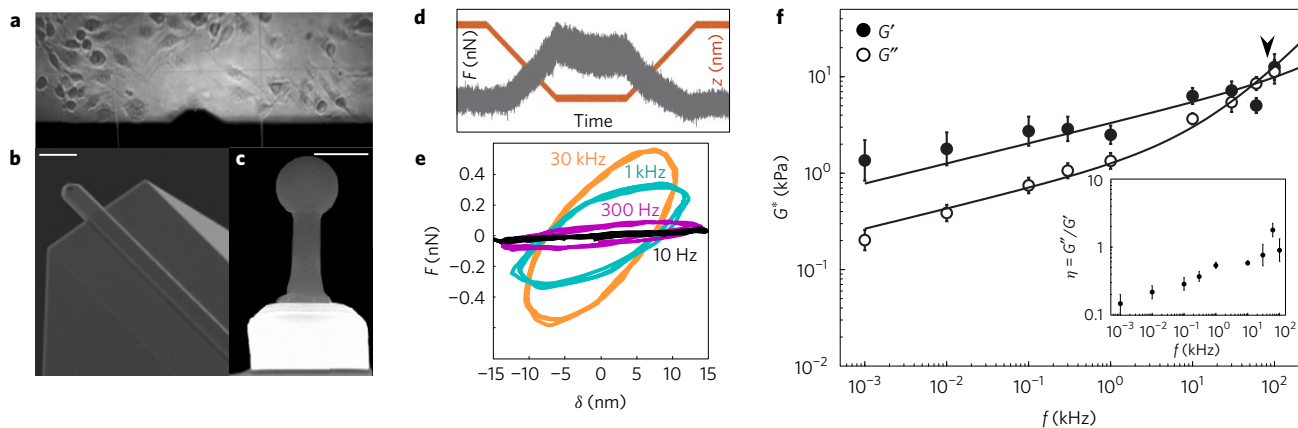


Figure 1 | High-frequency microrheology of living fibroblasts. **a**, Bright-field image of living 3T3 fibroblasts in the high-speed-AFM fluid chamber. **b**, Scanning electron micrograph of high-speed-AFM cantilever. Scale bar, 10 μm . Courtesy of NanoWorld USC Series, NanoWorld AG, Neuchâtel, Switzerland. **c**, Front view of the AFM cantilever showing the electron beam-deposited-spherical tip. Scale bar, 1 μm . **d**, Example of force-time trace with 1 kHz oscillation obtained on a living cell. At ~ 250 nm indentation, the contact time shows force-relaxation with the superimposed oscillation. The maximum force is ~ 0.5 nN. The red line shows piezo displacement (550 nm + 15-nm amplitude oscillation). **e**, Force-indentation loops obtained from the contact region of force curves at different oscillation frequencies, showing increased slope and hysteresis with frequency. **f**, Frequency dependence of the complex shear modulus $G^*(f) = G'(f) + iG''(f)$ of 3T3 cells ($N = 22$). Error bars represent the standard error of the mean of the log-transformed data. The arrowhead shows the transition frequency. Inset: loss tangent, $\eta = G''/G'$ as a function of frequency. Error bars represent the standard error of the mean.

Table 1 | Fitted parameters of a double power law and transition frequency* for the different treatments and cell types.

Cell	A (kPa)	α	B (kPa)	β	f_t (kHz)
Untreated 3T3s	3.48 ± 0.17	0.21 ± 0.01	0.15 ± 0.03	0.92 ± 0.03	84
+ Latrunculin-A	2.48 ± 0.27	0.20 ± 0.01	0.21 ± 0.06	0.94 ± 0.18	28
+ Blebbistatin	2.97 ± 0.38	0.24 ± 0.02	0.06 ± 0.02	1.21 ± 0.14	56
+ Calyculin-A	2.19 ± 0.38	0.09 ± 0.14	1.96 ± 0.38	0.38 ± 0.14	1.5
+ CK666	1.08 ± 0.13	0.09 ± 0.01	0.58 ± 0.09	0.59 ± 0.03	3.5
MCF10A (benign)	1.27 ± 0.26	0.27 ± 0.05	0.08 ± 0.28	0.93 ± 0.24	66
MCF7 (malignant)	0.14 ± 0.03	0.05 ± 0.02	1.77 ± 0.11	0.41 ± 0.01	10^{-3}

Errors represent the standard deviation (see Supplementary Information). *The transition frequency (f_t) was defined as the frequency at which $A(if_t)^\alpha = B(if_t)^\beta$, that is, $f_t = \exp(\frac{\ln(B) - \ln(A)}{\alpha - \beta})$.

effects^{27–29}, and at indentations 300 nm and with an oscillation amplitude of 15 nm, thus probing mainly the cortical cytoskeleton³⁰. Up to 300 Hz, both moduli increased with frequency at a similar rate, as shown by the increased slope and hysteresis of the force-indentation cycles (Fig. 1e) with $G'(f) > G''(f)$ and average loss tangent $\eta \sim 0.25$ (Fig. 1f, inset). Above 300 Hz, G'' grew at a faster rate, becoming larger than G' above 30 kHz. Accordingly, η increased from 0.37 at 300 Hz to 1.76 at 60 kHz. Various works using magnetic twisting cytometry and AFM have shown crossing of G'' over G' at frequencies ranging from 100 Hz to 1 kHz (refs 1,6,28). This apparent discrepancy might be explained by cytoskeleton remodelling around the probe, cell culture conditions or different mechanical response between cell types and cell regions (cell interior versus cortex), as passive microrheology suggests^{16,17}. Nevertheless, previous AFM and magnetic twisting cytometry measurements on 3T3 fibroblasts showed no crossover up to 1 kHz, in agreement with our results^{18,31}. Based on the experimental observation of a weak power law at low frequencies and a stronger power law at high frequencies supported by semiflexible filaments theories^{2,16,32}, G^* was modelled using a double power law $G^*(f/f_0) = A(if/f_0)^\alpha + B(if/f_0)^\beta$, where f_0 is an arbitrary frequency (1 Hz, in our case), A and B scaling factors, and α and β the low- and high-frequency exponents, respectively (see Supplementary Information). In particular, the exponent β is expected to be 1 for a purely viscous response, and 0.5, 0.75 or 0.875 if the transverse or longitudinal relaxation modes of the cytoskeleton filaments dominate⁷. Interestingly, for living 3T3 fibroblasts, the best fit to $G^*(f)$ resulted in a weak power law between 1 Hz and

1 kHz with an exponent $\alpha = 0.21 \pm 0.01$, where the response to mechanical deformations was mainly elastic (Fig. 1 and Table 1). At the newly accessible high-frequency regime (1 kHz–100 kHz), an exponent $\beta = 0.92 \pm 0.03$ described well the increasingly dominant contribution of $G''(f)$. We defined a transition frequency of 84 kHz, above which the strong power-law component became dominant (Table 1). Although other interpretations are plausible, for example, a purely viscous behaviour (see Supplementary Information), the exponent $\beta = 0.92$ is close to 0.875, predicted to originate from longitudinal relaxation modes of single cytoskeleton filaments tensed below a certain critical force^{14,33}. This scaling has been observed before on non-crosslinked actin solutions¹². This suggested that longitudinal modes of semiflexible filaments subjected to low tension dominate the mechanical response of the cortical cytoskeleton at short timescales.

To test whether the high-frequency response depends on the organization and state of the actin network, we treated cells with different drugs altering the structure and prestress of the actin cytoskeleton (Fig. 2 and Table 1). Actin disruption with Latrunculin-A (Fig. 2a) and Myosin II inhibition by Blebbistatin (Fig. 2b) had similar effects on fibroblasts. The elastic modulus decreased significantly at frequencies < 1 kHz, whereas the viscous modulus was not greatly affected. Instead, the high-frequency regime was characterized by increased viscous moduli. Compared to cells with intact cytoskeleton, the transition frequency was lower in cells with disrupted actin or reduced prestress (28 kHz and 56 kHz, respectively; compared to 84 kHz for untreated cells). In

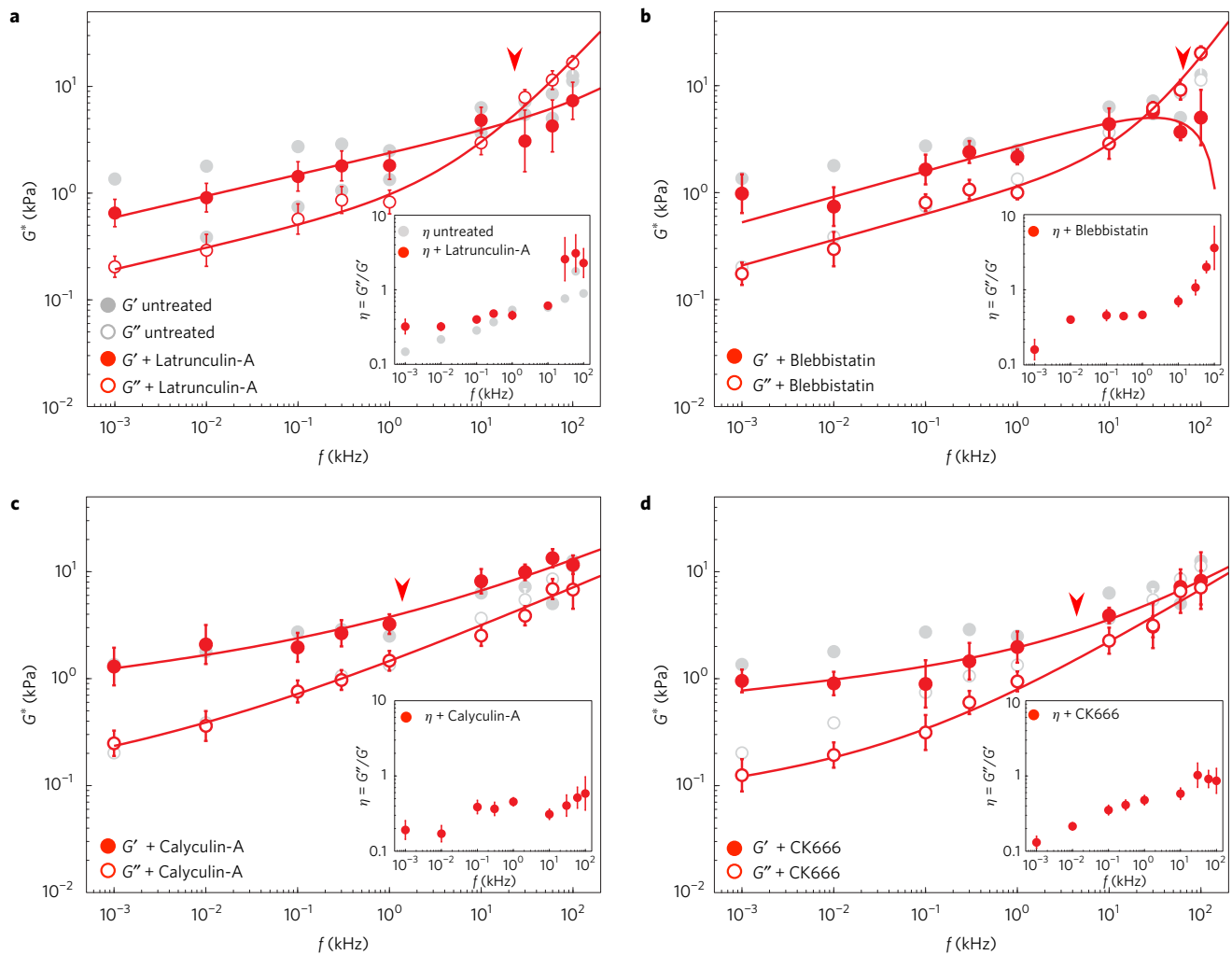


Figure 2 | High-frequency microrheology of fibroblasts with altered actin cytoskeleton. **a–d**, Frequency-dependent shear moduli and loss tangents (insets) for untreated cells (grey) and cells after cytoskeletal alterations (red). Arrowheads show the transition frequencies. **a**, Disruption of the actin cytoskeleton by Latrunculin-A ($N = 10$). **b**, Reduced prestress by Blebbistatin ($N = 8$). **c**, Increased prestress by Calyculin-A ($N = 13$). **d**, Actin branching inhibition by CK666 ($N = 6$). Solid lines represent the best fits of a double power law to treated cells. Fit parameters are shown in Table 1. Error bars in G^* represent the standard error of the mean of the log-transformed data. Error bars in η represent the standard error of the mean.

both treatments, the low-frequency regime showed a more fluid-like response than for untreated cells, whereas the high-frequency regime exhibited a purely viscous behaviour, indicated by $\beta \sim 1$ (0.94 for Latrunculin-A and 1.21 for Blebbistatin, Table 1). A physically meaningless exponent > 1 may suggest contributions not considered by single filament theories, such as poroelasticity, that may result in a more complex viscoelastic response, not fully described by a double power law. Interestingly, the loss tangent, η , was higher over the entire frequency range explored, indicating overall higher viscous stresses in treated than in untreated cells (Fig. 2a,b, inset). While at low frequencies this increase was due to a decreased G' , at high frequency the effect was mainly due to the increase of G'' . Thus, upon disruption of actomyosin cytoskeleton, the mechanical response at short timescales appeared dominated by the viscous cytoplasm. Increasing intracellular tension with Calyculin-A resulted in no substantial variation of the moduli at low frequencies (Fig. 2c). Noteworthy, at frequencies > 1 kHz, the measured elastic moduli increased, thus being larger than the viscous moduli over the whole dynamic range. Accordingly, an $\eta < 1$ underlined a prevalently elastic response of cells with increased prestress (Fig. 2c, inset). Furthermore, both exponents ($\alpha = 0.09$ and $\beta = 0.38$) were smaller than for untreated cells, reporting solid-like behaviour over the entire frequency range. The transition

frequency was 50 times lower (1.5 kHz) than on untreated cells; hence, the high-frequency response dominated over a much wider dynamic range. An exponent $\beta = 0.38$ compares to 0.5 observed on myosin II-prestressed actin networks^{11,15}. As predicted before, this suggests that prestress must be above a certain level to govern the fast viscoelastic response of living cells³³. Finally, we reduced actin crosslinking by inhibiting Arp2/3 with CK666, which induces architectural changes of the actin cortex from mesh-like to parallel arrangements³⁴. CK666 reduced both elastic and viscous moduli at low frequencies, while η remained similar to that of untreated cells (Fig. 2d). The high-frequency response resembled that of cells with increased prestress, with $G'(f) > G''(f)$, and a small η , but η close to one above 10 kHz. Noteworthy, the transition frequency was 25 times lower (3.5 kHz) than of untreated cells, again suggesting dominance of the high-frequency regime over a wide frequency range. The exponent $\beta = 0.59 \pm 0.03$ is compatible with prestressed filaments, suggesting that branching inhibition induced long filaments that result in softer cells at low frequencies, but a more elastic response than untreated cells at short timescales.

We thus hypothesized that cell types with different cytoskeletal properties exhibit distinctive behaviour at high frequencies. Hence, we compared the mechanics of benign (MCF10A) with malignant (MCF7) breast cancer cells. Previous works have shown that MCF7

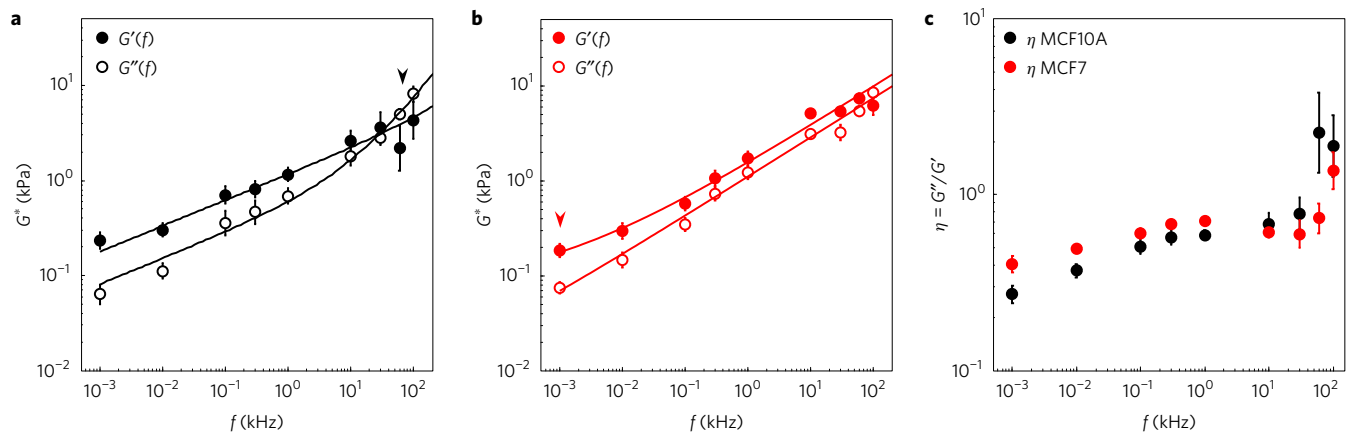


Figure 3 | High-frequency microrheology of benign and malignant cancer cells. **a, b**, Frequency-dependent shear moduli of benign (MCF10A, $N=9$) (**a**) and malignant (MCF7, $N=9$) cancer cells (**b**). Arrowheads show the transition frequencies. Solid lines represent the best fits of a double power law with parameters shown in Table 1. **c**, Frequency-dependent loss tangent $\eta = G''(f)/G'(f)$. Error bars in G^* represent the standard error of the mean of the log-transformed data. Error bars in η represent the standard error of the mean.

cells were more compliant and generated higher intracellular forces than MCF10A^{35,36}. Our high-frequency microrheology measurements revealed that both cell types have elastic moduli an order of magnitude lower than fibroblasts (0.1 kPa versus 1 kPa at 1 Hz), and a higher loss tangent η , indicating a more viscous behaviour. Recent active measurements on these same two cell types at frequencies <100 Hz are in excellent agreement with our results³⁶. However, MCF7 exhibited a different frequency response than MCF10A (Fig. 3a,b). The loss tangent of MCF10A weakly increased from 0.3 to 0.8 up to 30 kHz, and sharply shifted to ~ 2 above this frequency. Instead, malignant MCF7 cells exhibited a weaker increase of the loss tangent from 0.4 to 0.7 up to 60 kHz, always <1 except at 100 kHz (Fig. 3c). This implies that MCF7 were slightly more viscous at low frequencies, but more elastic at short timescales than MCF10A. Importantly, elastic stresses dominated over the whole frequency range in MCF7. At high frequencies, unlike MCF10A that showed a purely viscous response, but similar to fibroblasts with enhanced prestress (Fig. 2c), the G^* response of MCF7 was consistent with a tensed cytoskeleton network ($\beta = 0.41$, Table 1). Remarkably, as reflected by the much lower transition frequency of malignant MCF7 (~ 1 Hz) compared to that of MCF10A (66 kHz), the contribution of this tensed filament response dominated almost the entire dynamic range. In contrast, passive microrheology measurements at high frequencies have recently shown similar viscoelastic responses for MCF7 and MCF10A, both consistent with an exponent of 0.75 (ref. 37). As has been suggested before, it is likely that passive methods probe the intracellular network, while AFM probes the cortical cytoskeleton¹⁶. The dramatic difference we observe between the transition frequency and the scaling laws at high frequency of malignant and benign cells cortex suggests a possible marker of the metastatic state, more discernible than the absolute magnitude of an elastic modulus.

Thanks to the wide accessible frequency range we were able to identify two viscoelastic regimes: a low-frequency regime where the structural elements of the cell cytoskeleton at the mesoscale seem to dominate the viscoelastic response, and a high-frequency regime in which the response is well described by single filament theories. Our data show that the mechanical response to high-frequency deformations is richer than previously suggested and reflects the morphological and dynamical state of the cytoskeleton. Although known theories do predict some of the observed frequency responses, deeper understanding may require taking into account the complex molecular nature of cytoskeletal elements³⁸, such as the rate-dependent mechanical response of individual proteins²². We expect that probing cell viscoelasticity at the now-accessible

frequency range will stimulate the development of such refined theories. Moreover, combination of our approach with passive microrheology will allow us to assess if the cell is in thermal equilibrium at the now accessible short timescales, as some works suggest^{39–41}. Finally, high-frequency microrheology opens the door towards a univocal characterization of the mechanical phenotype of living cells, and is likely to provide new insights into other soft matter systems such as biopolymer gels and emulsions.

Methods

Methods, including statements of data availability and any associated accession codes and references, are available in the [online version of this paper](#).

Received 5 October 2016; accepted 21 March 2017;
published online 1 May 2017

References

1. Fabry, B. *et al.* Scaling the microrheology of living cells. *Phys. Rev. Lett.* **87**, 148102–148105 (2001).
2. Deng, L. H. *et al.* Fast and slow dynamics of the cytoskeleton. *Nat. Mater.* **5**, 636–640 (2006).
3. Petersen, N. O., McConnaughey, W. B. & Elson, E. L. Dependence of locally measured cellular deformability on position on the cell, temperature, and cytochalasin B. *Proc. Natl Acad. Sci. USA* **79**, 5327–5331 (1982).
4. Kollmannsberger, P. & Fabry, B. Linear and nonlinear rheology of living cells. *Annu. Rev. Mater. Res.* **41**, 75–97 (2011).
5. Bausch, A. & Kroy, K. A bottom-up approach to cell mechanics. *Nat. Phys.* **2**, 231–238 (2006).
6. Alcaraz, J. *et al.* Microrheology of human lung epithelial cells measured by atomic force microscopy. *Biophys. J.* **84**, 2071–2079 (2003).
7. Broedersz, C. P. & MacKintosh, F. C. Modeling semiflexible polymer networks. *Rev. Mod. Phys.* **86**, 995–1036 (2014).
8. Gittes, F. *et al.* Microscopic viscoelasticity: shear moduli of soft materials determined from thermal fluctuations. *Phys. Rev. Lett.* **79**, 3286–3289 (1997).
9. Amblard, F. *et al.* Subdiffusion and anomalous local viscoelasticity in actin networks. *Phys. Rev. Lett.* **77**, 4470–4473 (1996).
10. Isambert, H. & Maggs, A. Dynamics and rheology of actin solutions. *Macromolecules* **29**, 1036–1040 (1996).
11. Caspi, A., Elbaum, M., Granek, R., Lachish, A. & Zbaida, D. Semiflexible polymer network: a view from inside. *Phys. Rev. Lett.* **80**, 1106–1109 (1998).
12. Koenderink, G. H., Atakhorrami, M., MacKintosh, F. C. & Schmidt, C. F. High-frequency stress relaxation in semiflexible polymer solutions and networks. *Phys. Rev. Lett.* **96**, 138307 (2006).
13. Semmrich, C. Glass transition and rheological redundancy in F-actin solutions. *Proc. Natl Acad. Sci. USA* **104**, 20199–20203 (2007).
14. Everaers, R., Jülicher, F., Ajdari, A. & Maggs, A. C. Dynamic fluctuations of semiflexible filaments. *Phys. Rev. Lett.* **82**, 3717–3720 (1999).
15. Mizuno, D., Tardin, C., Schmidt, C. F. & MacKintosh, F. C. Nonequilibrium mechanics of active cytoskeletal networks. *Science* **315**, 370–373 (2007).

16. Hoffman, B. D., Massiera, G., Van Citters, K. M. & Crocker, J. C. The consensus mechanics of cultured mammalian cells. *Proc. Natl Acad. Sci. USA* **103**, 10259–10264 (2006).
17. Yamada, S., Wirtz, D. & Kuo, S. C. Mechanics of living cells measured by laser tracking microrheology. *Biophys. J.* **78**, 1736–1747 (2000).
18. Mahaffy, R. E., Shih, C. K., MacKintosh, F. C. & Kas, J. Scanning probe-based frequency-dependent microrheology of polymer gels and biological cells. *Phys. Rev. Lett.* **85**, 880–883 (2000).
19. Cartagena-Rivera, A. X., Wang, W.-H., Geahlen, R.L. & Raman, A. Fast, multi-frequency, and quantitative nanomechanical mapping of live cells using the atomic force microscope. *Sci. Rep.* **5**, 11692 (2015).
20. Gavara, N. & Chadwick, R. S. Noncontact microrheology at acoustic frequencies using frequency-modulated atomic force microscopy. *Nat. Methods* **7**, 650–654 (2010).
21. Ando, T. *et al.* A high-speed atomic force microscope for studying biological macromolecules. *Proc. Natl Acad. Sci. USA* **98**, 12468–12472 (2001).
22. Rico, F., Gonzalez, L., Casuso, I., Puig-Vidal, M. & Scheuring, S. High-speed force spectroscopy unfolds titin at the velocity of molecular dynamics simulations. *Science* **342**, 741–743 (2013).
23. Alcaraz, J. *et al.* Correction of microrheological measurements of soft samples with atomic force microscopy for the hydrodynamic drag on the cantilever. *Langmuir* **18**, 716–721 (2002).
24. Janovjak, H. J., Struckmeier, J. & Muller, D. J. Hydrodynamic effects in fast AFM single-molecule force measurements. *Eur. Biophys. J. Biophys. Lett.* **34**, 91–96 (2005).
25. Schnurr, B., Gittes, F., MacKintosh, F. & Schmidt, C. Determining microscopic viscoelasticity in flexible and semiflexible polymer networks from thermal fluctuations. *Macromolecules* **30**, 7781–7792 (1997).
26. Colom, A., Casuso, I., Rico, F. & Scheuring, S. A hybrid high-speed atomic force–optical microscope for visualizing single membrane proteins on eukaryotic cells. *Nat. Commun.* **4**, 2155 (2013).
27. Gavara, N. & Chadwick, R. S. Determination of the elastic moduli of thin samples and adherent cells using conical atomic force microscope tips. *Nat. Nanotech.* **7**, 733–736 (2012).
28. Takahashi, R. & Okajima, T. Mapping power-law rheology of living cells using multi-frequency force modulation atomic force microscopy. *Appl. Phys. Lett.* **107**, 173702 (2015).
29. Rigato, A., Rico, F., Eghiaian, F., Piel, M. & Scheuring, S. Atomic force microscopy mechanical mapping of micropatterned cells shows adhesion geometry-dependent mechanical response on local and global scales. *ACS Nano* **9**, 5846–5856 (2015).
30. Clark, A. G., Dierkes, K. & Paluch, E. K. Monitoring actin cortex thickness in live cells. *Biophys. J.* **105**, 570–580 (2013).
31. Zhou, E., Quek, S. & Lim, C. Power-law rheology analysis of cells undergoing micropipette aspiration. *Biomech. Model. Mechanobiol.* **9**, 563–572 (2010).
32. Fabry, B. *et al.* Time scale and other invariants of integrative mechanical behavior in living cells. *Phys. Rev. E* **68**, 041914 (2003).
33. Obermayer, B. & Frey, E. Tension dynamics and viscoelasticity of extensible wormlike chains. *Phys. Rev. E* **80**, 040801 (2009).
34. Eghiaian, F., Rigato, A. & Scheuring, S. Structural, mechanical, and dynamical variability of the actin cortex in living cells. *Biophys. J.* **108**, 1330–1340 (2015).
35. Guck, J. *et al.* Optical deformability as an inherent cell marker for testing malignant transformation and metastatic competence. *Biophys. J.* **88**, 3689–3698 (2005).
36. Guo, M. *et al.* Probing the stochastic, motor-driven properties of the cytoplasm using force spectrum microscopy. *Cell* **158**, 822–832 (2014).
37. Bertseva, E. Optical trapping microrheology in cultured human cells. *Eur. Phys. J. E* **35**, 1–8 (2012).
38. Kroy, K. & Glaser, J. The glassy wormlike chain. *New J. Phys.* **9**, 416 (2007).
39. Ahmed, W. W. *et al.* Active mechanics reveal molecular-scale force kinetics in living oocytes. Preprint at <http://arXiv.org/abs/151008299> (2015).
40. Bursac, P. *et al.* Cytoskeletal remodelling and slow dynamics in the living cell. *Nat. Mater.* **4**, 557–561 (2005).
41. Turlier, H. *et al.* Equilibrium physics breakdown reveals the active nature of red blood cell flickering. *Nat. Phys.* **12**, 513–519 (2016).

Acknowledgements

The authors thank A. Sergé, M. Lopez and N. Dusetti for generously providing cell lines and for their technical support, L. Borge from the PCC TPR2-Luminy for technical assistance and F. Eghiaian for helpful discussions. This work was supported by Agence National de la Recherche grants *BioHSFS* ANR-15-CE11-0007, ANR-11-LABX-0054 (Labex INFORM), ANR-11-IDEX-0001-02 (A*MIDEX) and a European Research Council (ERC) Grant #310080 (MEM-STRUCT-AFM).

Author contributions

A.R. designed and performed the experiments, analysed the data and wrote the manuscript. F.R. designed the experiments, analysed the data and wrote the manuscript. A.M. modified the high-speed-AFM scanner and helped with calibration and experiments. S.S. contributed to designing the experiments and writing the manuscript.

Additional information

Supplementary information is available in the online version of the paper. Reprints and permissions information is available online at www.nature.com/reprints. Publisher's note: Springer Nature remains neutral with regard to jurisdictional claims in published maps and institutional affiliations. Correspondence and requests for materials should be addressed to F.R.

Competing financial interests

The authors declare no competing financial interests.

Methods

Cell culture. NIH-3T3 fibroblasts (ATCC) were cultured in Dulbecco's Modified Eagle Medium (DMEM; Gibco) supplied with 10% Bovine Serum Albumin (BSA; Gibco) and split at 80% confluence. They were detached using Ethylenediaminetetraacetic acid (EDTA) 0.02% in phosphate buffered saline (PBS) (Versene Solution, Gibco). MCF7 (ATCC HTB-22) were cultured in DMEM supplied with 0.01 mg ml⁻¹ human recombinant insulin (Sigma, I2643) and 10% BSA (Gibco). MCF10A (ATCC CRL-10317) were cultured in Mammary Epithelial Basal Medium (MEBM; Promocell C-21010) supplemented with Bovine Pituitary Extract 0.004 ml ml⁻¹, Epidermal Growth Factor (recombinant human) 10 ng ml⁻¹, human recombinant insulin 10 µg ml⁻¹, hydrocortisone 0.5 µg ml⁻¹ (Promocell SupplementPack C-39110) and 100 ng ml⁻¹ Cholera Toxin (Sigma, C8052). For AFM measurements, cells were grown overnight (20–30% confluence) on glass rods of 1 mm diameter coated with fibronectin (Sigma, F1141). Small and light glass rods are required to fit the small dimensions of the piezo elements (2 mm × 2 mm) and to prevent changes in the piezo response.

Drug treatments. All drugs were dissolved in dimethyl sulfoxide (DMSO), then diluted in Hank's Balanced Salt Solution (Gibco 14170120) before experiments. Drugs were directly added to the fluid chamber of the AFM from a mother solution to reach the desired concentration. The final concentrations were: Blebbistatin (Myosin inhibitor, Sigma B0560), 20 µM; Latrunculin-A (Actin disruptor, Sigma L5163), 500 nM; Calyculin-A (contractility agonist, Sigma 21279), 50 µM; CK666 (Arp2/3 inhibitor, Sigma SML0006), 50 µM.

High-speed AFM measurements. Microrheology measurements were performed with a modified high-speed AFM (RIBM) equipped with a high-frequency function generator (33500B, Keysight), 100 MHz-bandwidth acquisition board and computer (PXI/PCI-5122, National Instruments) interfaced with home-built software developed in Labview. We adapted high-speed-AFM (ref. 21) with a miniature piezoelectric element of high resonance frequency (200 kHz, see Supplementary Fig. 2). High-frequency microrheology measurements were carried out in Hank's balanced salt solution (Gibco) at room temperature. To account for evaporation, the solution was exchanged every 10 min (that is, the time necessary to measure one cell). Cells were grown on glass cylinders of 1.5 mm height and 1 mm diameter. The cylinder was then mounted on the *z*-piezo, on top of a prism which allows transmitted illumination of the sample²⁶. We used NW-USC-F1.2-k0.15-B500 microcantilevers (Nanoworld), with nominal spring constant of 0.15 nN nm⁻¹, resonance frequency of 1.2 MHz in air and ~600 kHz in liquid, and reduced viscous drag (4 × 10⁻⁵ nN ms nm⁻¹). At the end of the cantilevers, a tip was grown by electron beam deposition featuring a sphere of 1 µm diameter, reducing the viscous damping effect near the solid support and minimizing the change in the resonance frequency by the added mass (Fig. 1a–c). To reduce unspecific adhesion between the cantilever tip and the cell surface, tips were incubated at room temperature with Pluronic 0.01% for 10 min. Pluronic 0.01% was also added to the cell medium to further prevent tip contamination. The calibration of the spring constant and the deflection sensitivity was done using the Sader method for each cantilever and each experiment^{42,43}. The deflection sensitivity was calibrated before and after measuring each cell by recording the thermal spectrum and using the calibrated spring constant. The signal in liquid was corrected for the effects of the different oscillation modes of the cantilever and the tilting angle⁴⁴. For engaging, we set a deflection setpoint of ~400 pN. Measurements were carried out around the perinuclear region to minimize variability and avoid influence of the hard substrate²⁹. The possible effect of the cell tilt angle within the perinuclear region was estimated to be <6% (<20° angle) and ~3% on average, much smaller than the intracellular variability^{28,45}. Force curves were carried out with a ramp size of 550 nm, with approach and retract velocity of 5.5 µm s⁻¹. Simultaneously, a sinusoidal signal of 15-nm amplitude was added to the piezo movement using a function generator. Small-amplitude oscillation was used to assure linear response of the cell and minimize ageing of the piezo. Oscillatory measurements were performed in the frequency range 1 Hz–100 kHz, at an operating indentation <300 nm. The indentation was kept constant for a variable time according to the frequency applied, from a minimum of 10 ms at 100 kHz to a maximum of 10 s at 1 Hz oscillation frequency (Supplementary Fig. 1). The change in the indentation due to stress relaxation of the cell (change in deflection <3 nm) was <1%, resulting in a negligible change in the contact area. Measurements at different frequencies were performed in random order.

Characterization of the *z*-piezo. To characterize the amplitude and phase response of the *z*-piezo, we acquired force curves in liquid with a superposed oscillation on the glass surface of each sample, at all frequencies used to measure cells. This characterization was carried out at the end of each experiment on a clean, bare region near the probed cells; thus, on the exact same sample supports, and using the same amplitudes as during the measurements. Since, in some cases, the bare glass was not clean enough for calibration, the average phase delay from all calibrations, φ , was calculated and used to correct the measurements on cells

(Supplementary Fig. 2A). Because the oscillation amplitude increases when the driving frequency approaches the mechanical resonance of the piezo, we measured the real oscillation amplitude of the piezo at all frequencies used (Supplementary Fig. 2B), and subsequently corrected the input signal recorded by the acquisition board. The voltage sent to the piezo was adjusted to obtain always the same oscillation amplitude of 15 nm. The low variability in the piezo response confirmed that ageing of the piezo was negligible.

Viscous drag calculation. We estimated the viscous drag acting on the cantilever at contact by recording the deflection of the cantilever at different distances from the surface due to 15-nm amplitude oscillations of the *z*-piezo, as described by Alcaraz and colleagues²³. The drag transfer function was thus computed as: $H_d(f) = F(f)/\delta(f)e^{-i\varphi}$, where $F(f)$ and $\delta(f)$ are the Fourier transform of the force and indentation, respectively, f is the driving frequency, and φ is the phase delay of the piezo. The drag factor B was then calculated as $B(h) = H_d/(2\pi f)$ (Supplementary Fig. 3B). The drag factor at contact was thus extrapolated at the intercept at $h=0$. The value of $B(0)$ obtained on glass was of 4.0×10^{-5} nN ms nm⁻¹. To estimate $B(0)$ on cells, where the uncertainty in the determination of the point of contact is important, we exploited the non-contact part of the force curves, and obtained values between 2.5 and 3.5×10^{-5} nN ms nm⁻¹ (Supplementary Fig. 3B). An average value of 3.0×10^{-5} nN ms nm⁻¹ was then used to correct for the viscous drag contribution of the cantilever.

Data processing. Data were processed using custom programs written in Matlab 2013a (Mathworks). Briefly, force curves showing an indentation <300 nm and maximum force of ~1 nN were used. Only the force–displacement loops with coherence higher than 0.9 between the force and *z*-signals were selected for subsequent analysis. The full contact region was then windowed with a Hamming window and the force-relaxation separated from the oscillation by moving-average filtering.

The complex modulus $G^*(f)$ was calculated from the force–indentation (F – δ) loops in the contact region by Fourier analysis, similarly to the method used by Alcaraz and colleagues⁶. Briefly, the total transfer function is derived by transforming the equation of motion of the cantilever into the frequency domain, and dividing it by the indentation, as explained in ref. 23. The resulting equation for the total transfer function was computed as: $H_{\text{tot}}(f) = F(f)/\delta(f)e^{-i\varphi}$, where $F(f)$ and $\delta(f)$ are the Fourier transforms of the force and deflection, respectively, and $i\varphi$ is the delay of the piezoactuator. The transfer function of the sample was calculated as

$$H_s = H_{\text{tot}} \left(1 - \left(\frac{f}{f_R} \right)^2 \right) - H_d$$

where f_R is the resonant frequency of the cantilever, and $H_d = B(0) \cdot 2\pi f$. Because at the highest frequencies f is ~1/5 of f_R , we did not neglect the term $(f/f_R)^2$ as done in previous works at lower frequencies²³. We then computed the complex shear modulus from the Taylor expansion of the Hertz model of a rigid sphere indenting an elastic half space, as

$$G^*(f) = H_s(f) \cdot \frac{1 - \nu}{4 \cdot \sqrt{R} \cdot \delta_0}$$

where ν is Poisson's ratio (assumed 0.5), δ_0 the operating indentation (~300 nm), and R the tip radius (500 nm)^{6,18}.

Data analysis and statistics. Due to the log-normal distribution of the shear modulus (Supplementary Fig. 7), average values for $G^*(f)$ at each frequency (Figs 1e, 2 and 3) correspond to the geometric mean of the values obtained on each single cell. Error bars represent the standard error of the mean of the log-transformed data. The average values were fitted to a double power law:

$$G'(f) = A \cos(\pi\alpha/2)f^\alpha + B \cos(\pi\beta/2)f^\beta$$

$$G''(f) = A \sin(\pi\alpha/2)f^\alpha + B \sin(\pi\beta/2)f^\beta$$

by chi-square (χ^2) minimization of the log-transformed data, leaving the four parameters, A , B , α and β , free. Errors on the fitted parameters were estimated using jackknife resampling. Briefly, for each condition we repeated the computation of the average $G^*(f)$ as many times as the number of cells, each time excluding one set of measurements. We thus fitted each average $G^*(f)$ to the double power-law model and obtained A , B , α and β for each resampling. The errors on the parameters report the standard deviation of the parameters obtained from all the fits⁴⁶.

To assess the reliability of the fitted model, we repeated the fit of $G^*(f)$ for the data set by fixing one exponent: $\alpha = 0$, $\beta = 1/2$, $\beta = 3/4$, $\beta = 7/8$, $\beta = 1$ (Supplementary Table 1). From the minimized χ^2 of each fit, we computed the cumulative probability (p) of a chi-square distribution with that particular χ^2 value and $N-M$ degrees of freedom, M being the number of data points and N the

number of fitted parameters. The complement of p , $q = 1 - p$, provides a quantitative estimation of the goodness of the fit for each model⁴⁶. Obviously, the chi-square value was always the lowest when leaving all parameters free (Supplementary Table 1). Except for the model assuming a flat plateau at low frequencies, all models provided q values similarly close to 1. Thus, for consistency, we opted for reporting all the values obtained by unconstrained fitting of the double power-law model. Nonetheless, we interpreted the fitted β exponent in terms of one of the available theories—thus, assuming a fixed β value. All data processing and analysis were performed in Matlab 2013a (Mathworks).

Data availability. The data that support the plots within this paper and other findings of this study are available from the corresponding author upon request.

References

42. Higgins, M. J. *et al.* Noninvasive determination of optical lever sensitivity in atomic force microscopy. *Rev. Sci. Instrum.* **77**, 013701 (2006).
43. Sader, J. E., Chon, J. W. M. & Mulvaney, P. Calibration of rectangular atomic force microscope cantilevers. *Rev. Sci. Instrum.* **70**, 3967–3969 (1999).
44. Hutter, J. L. Comment on tilt of atomic force microscope cantilevers: effect on spring constant and adhesion measurements. *Langmuir* **21**, 2630–2632 (2005).
45. Rico, F. *et al.* Probing mechanical properties of living cells by atomic force microscopy with blunted pyramidal cantilever tips. *Phys. Rev. E. Stat. Nonlin. Soft Matter Phys.* **72**, 021914 (2005).
46. Press, W. H. *Numerical Recipes 3rd Edition: The Art of Scientific Computing* (Cambridge Univ. Press, 2007).